Chapter 13
Application of Nonlinear Viscoelastic Material Models for the Shrinkage and Warpage Analysis of Blow Molded Parts

Patrick Michels, Christian Dresbach, Esther Ramakers-van Dorp, Holm Altenbach, and Olaf Bruch

Abstract The prediction of shrinkage and warpage of extrusion blow molded plastic parts is a topic of high industrial demand. Nevertheless, simulation results are still associated with uncertainties. One of the major difficulties is the description of the complex time-, temperature- and process-dependent material behavior of semi-crystalline polymers like high density polyethylene (HDPE). It is state of the art to use linear viscoelastic material models for the shrinkage and warpage analysis. However, linear viscoelastic behavior can only be assumed if the stresses are small. To increase the prediction accuracy of the current simulation models, nonlinear viscoelastic material models, such as the Abaqus Parallel Rheological Framework (PRF), are investigated. The calibration of the PRF model can be quite challenging, especially if a higher number of networks is used. Consequently, we present a calibration strategy that uses functional relations to describe the parameters along the network elements in order to reduce the dimensions of the design space for model calibration. To find the best possible solution, the global optimization algorithm Adaptive Simulated Annealing (ASA) is used. A simplified one-dimensional representation of the PRF model is implemented in Matlab to further reduce the computational effort of the

Patrick Michels
Bonn-Rhein-Sieg University of Applied Sciences, Grantham Allee 20, 53757 Sankt Augustin, Germany,
e-mail: patrick.michels@h-brs.de

Christian Dresbach · Esther Ramakers-van Dorp
Bonn-Rhein-Sieg University of Applied Sciences, Von-Liebig-Str. 20, 53359 Rheinbach, Germany,
e-mail: christian.dresbach@h-brs.de, esther.vandorp@h-brs.de

Holm Altenbach
Otto von Guericke University Magdeburg, Universitätsplatz 2, 39106 Magdeburg, Germany, e-mail: holm.altenbach@ovgu.de

Olaf Bruch
Dr. Reinold Hagen Stiftung, Kautexstr. 53, 53229 Bonn & Bonn-Rhein-Sieg University of Applied Sciences, Grantham Allee 20, 53757 Sankt Augustin, Germany,
e-mail: o.bruch@hagen-stiftung.de, olaf.bruch@h-brs.de

H. Altenbach and K. Naumenko (eds.), *Creep in Structures VI*,
Advanced Structured Materials 194, https://doi.org/10.1007/978-3-031-39070-8_13

model calibration. The calibration workflow is successfully tested using a set of relaxation tests with subsequent unloading at different strain and temperature levels. A good agreement between the experimental material tests and the simulation results, using the calibrated PRF model, is observed.

13.1 Introduction

The extrusion blow molding process is one of the most economic methods for the production of hollow plastic parts like bottles, cans, fuel tanks and large containers. The process itself can be divided into three main steps. In the first step a hollow tube, which is called parison, is extruded. Once the parison has reached its final length, the mold closes and the parison is inflated against the walls of the cooled mold. The blowing pressure is then maintained until the part solidifies. During the cooling under mold constraint, thermal stresses build up which lead to shrinkage and warpage of the final part after demolding. These undesired shape deviations cause major problems for the blow molding industry. In general, higher demolding temperatures lead to higher shrinkage and warpage, whereas lower demolding temperatures lead to a higher amount of residual stresses. In practice, there are several ways to deal with these difficulties. First, the cooling time can be increased, which leads to a higher amount of residual stresses and in most cases to an uneconomical production. On the other hand, the part warpage can be reduced by specific changes to the mold design. In the latter case, the use of Computer Aided Engineering (CAE) methods at an early stage of the product development offers great potential. Nevertheless, the prediction of the process-related shrinkage and warpage is still associated with uncertainties. One of the major difficulties is the modeling of the complex time-, temperature- and process-dependent material behavior of semi-crystalline polymers like HDPE. During processing, the polymer passes various stages in which its mechanical and thermal behavior drastically changes. The extrusion and inflation takes place at temperatures above the crystallite melting temperature T_m. In this temperature range, the material can be assumed as an amorphous melt with low structural stiffness. Below T_m the material behaves like a thermo-viscoelastic solid.

In literature, only a few research groups have dealt with the shrinkage and warpage analysis of blow molded parts. A first simulation approach considering the complete blow molding process including parison formation, clamping, inflation, solidification, and warpage was introduced by Laroche et al. [1]. They assumed the material to behave like an isotropic thermorheologically simple solid during the cooling. A linear viscoelastic material model (fluid-like generalized Maxwell) with three relaxation times was used in conjunction with the reduced time concept to model the temperature dependency [1, 2]. The shift function was approximated by the WLF-equation according to Williams, Landel and Ferry [3]. A good qualitative agreement between the warpage simulation and experimental measurements of a plastic fuel tank (PFT) was observed. Debergue et al. [4] investigated the influence of a small and large displacement approach on the warpage analysis of a blow molded

automotive part. A fluid-like generalized Maxwell model with 4 relaxation times was used. The investigation showed that the large displacement approach played a rather subordinate role in the warpage analysis. In contrast, the authors stated that part positioning after demolding in conjunction with gravity plays a critical role for the shrinkage and warpage prediction. A comparison of the simulation results with experimental warpage measurements under varying process conditions showed inaccuracies both qualitatively and quantitatively. Further investigations based on a fluid-like generalized Maxwell model with six relaxation times were carried out by Benrabah et al. [5]. The main focus of their investigation was the influence of deflashing on the component warpage. In [6], the implementation of a solid-like generalized Maxwell model was presented and compared to the fluid-like model. The warpage deformation of the solid-like model was less than the deformation of the fluid-like model, which the authors suggested was due to the lower structural stiffness of the fluid like model below the melting temperature. Finally, in a validation case study Benrabah et al. [7] observed a good qualitative agreement between the warpage simulation and experimental measurements of a blow molded PFT. A fluid-like generalized Maxwell model with five relaxation times was used for the analysis.

In [8], the shrinkage behavior of simple blow molded parts was investigated under varying process conditions and compared to simulation results. Anisotropic shrinkage behavior of the investigated parts was observed at which the level of anisotropy increased with higher degrees of stretching. Experimental measurements of Ramakers-van Dorp et al. [9] and Grommes et al. [10] on extrusion blow molded parts showed a rather small anisotropy of the elastic modulus, whereas experiments of Ramakers-van Dorp [11] showed a pronounced anisotropy of the coefficient of thermal expansion (CTE). Consequently, an isotropic generalized Maxwell solid model with 19 relaxation times in conjunction with the WLF-equation and orthotropic process- and temperature-dependent CTE was used in [8]. The simulation results matched the anisotropic shrinkage values reasonably well.

In summary, the use of linear viscoelastic models can be seen as state of the art for the shrinkage and warpage simulation of blow molded parts. However, in case of semi-crystalline polymers like HDPE, linear viscoelastic material behavior can only be assumed for small stresses and strains. At higher stresses and strains, HDPE reacts nonlinear viscoelastically. Creep experiments of Lai and Bakker [12] on HDPE samples indicate a strong nonlinear behavior even at very small stresses. They suggested that linearity exists only at vanishing small stresses [12]. In literature, several constitutive equations for the description of nonlinear viscoelastic material behavior are presented, among others in [13–16]. But only recently, nonlinear viscoelastic models like the Abaqus (Dassault Systèms) PRF model [16–18] have become available as standard in commercial finite element software products. However, the use of these models in the shrinkage and warpage analysis is quite challenging. To cover the extensive time and temperature range of the shrinkage and warpage analysis, the model calibration might involve a huge number of material parameters which need to be identified. Consequently, we present a calibration strategy which reduces the dimension of the design space by the use of functional relations between the material parameters. The Abaqus nonlinear viscoelastic PRF model is used, but the general

procedure can also be applied to similar models like the Parallel Network (PN) model [19] which is provided by the PolyUMod library (PolymerFEM LLC) [20].

13.2 Material Models

In this study, the Abaqus Parallel Rheological Framework model will be integrated into the shrinkage and warpage anlysis presented in [8] and compared with the linear viscoelastic model. In the following, the basic equations and the most important features of the material models will be discussed. We start with the linear viscoelastic model implemented in Abaqus which has already been used in [8]. Thereafter, the nonlinear viscoelastic PRF model will be discussed.

13.2.1 Linear Viscoelastic Material Model

The stress response of a linear viscoelastic material can be described by the following integral equation:

$$\sigma(t) = \int_0^t E_\mathrm{R}(t-s)\,\dot{\varepsilon}(s)\,\mathrm{d}s, \tag{13.1}$$

where $\sigma(t)$ is the stress at time t, $\dot{\varepsilon}$ is the strain rate and $E_\mathrm{R}(t)$ is the time dependent relaxation modulus. The relaxation modulus is often used in a normalized form so that we obtain:

$$\sigma(t) = E \int_0^t g_\mathrm{R}(t-s)\,\dot{\varepsilon}(s)\,\mathrm{d}s, \tag{13.2}$$

where E is the instantaneous modulus and $g_\mathrm{R}(t)$ is the dimensionless relaxation function. In Abaqus, the normalized relaxation function $g_\mathrm{R}(t)$ is approximated by a Prony series [18]

$$g_\mathrm{R}(t) = \frac{E_\mathrm{R}(t)}{E} = 1 - \sum_{i=1}^{N} g_i\,(1 - e^{-t/\tau_i}). \tag{13.3}$$

In Eq. (13.3) g_i and τ_i are material parameters, the so called Prony values and relaxation times. Assuming isotropic material behavior, Eq. (13.2) can be generalized to multiaxial loading by separating the strain tensor $\boldsymbol{\varepsilon}$ into deviatoric and volumetric parts. For the time dependent Cauchy stress tensor, $\boldsymbol{\sigma}$ applies [19]:

$$\boldsymbol{\sigma}(t) = 2G \int_0^t g_\mathrm{R}(t-s)\,\dot{\boldsymbol{\varepsilon}}_\mathrm{dev}(s)\,\mathrm{d}s + K \int_0^t \kappa_\mathrm{R}(t-s)\,\dot{\boldsymbol{\varepsilon}}_\mathrm{vol}(s)\,\mathrm{d}s, \tag{13.4}$$

with the instantaneous shear modulus G, the normalized shear relaxation function $g_R(t)$, the instantaneous bulk modulus K, the normalized bulk relaxation function $\kappa_R(t)$, and the time derivatives of the deviatoric $\boldsymbol{\varepsilon}_{dev}$ and volumetric $\boldsymbol{\varepsilon}_{vol}$ parts of the strain tensor $\boldsymbol{\varepsilon}$. Thus, the three-dimensional material behavior can be defined by two independent relaxation functions, the shear relaxation function, and the bulk relaxation function.

Temperature effects can be included by the use of the time temperature superposition (TTS). Therefore, the reduced time $\xi(t)$ is used in Eq. (13.5) [18]

$$\boldsymbol{\sigma}(t) = 2G \int_0^t g_R(\xi(t) - \xi(s))\, \dot{\boldsymbol{\varepsilon}}_{dev}(s)\, \mathrm{d}s + K \int_0^t \kappa_R(\xi(t) - \xi(s))\, \dot{\boldsymbol{\varepsilon}}_{vol}(s)\, \mathrm{d}s. \quad (13.5)$$

The reduced time is defined by [18]:

$$\xi(t) = \int_0^t \frac{\mathrm{d}s}{\alpha(\theta(s))}, \quad (13.6)$$

where $\alpha(\theta(t))$ is the shift function which can be approximated using the WLF equation (Eq. (13.7)) or the Arrhenius equation (Eq. (13.8))

$$\log_{10}(\alpha) = -\frac{C_1(\theta - \theta_{Ref})}{C_2 + (\theta - \theta_{Ref})}, \quad (13.7)$$

$$\ln(\alpha) = \frac{E_A}{R}\left(\frac{1}{T} - \frac{1}{T_{Ref}}\right). \quad (13.8)$$

The variables C_1 and C_2 are material parameters, E_A is the activation energy, R the universal gas constant, θ the temperature, and θ_{Ref} the reference temperature. For the Arrhenius equation the temperatures T and T_{Ref} must be specified in Kelvin. In addition, the instantaneous modulus can also be defined as a function of temperature [18].

To define thermal expansion behavior of the linear viscoelastic model, Abaqus allows the use of isotropic and orthotropic thermal expansion coefficients which can be constant or a function of temperature and field variables [18].

Instead of the previously described integral equation, the linear viscoelastic material model can also be derived by differential equations, which in fact is equivalent to the integral form [19]. The differential form is often used to build rheological models, which can be constructed using simple rheological spring and dashpot elements. Therefore, the linear viscoelastic model defined by the Prony series (Eq. (13.3)) is equivalent to a generalized Maxwell model (Fig. 13.1) [19]. It consists of an arbitrary number of Maxwell elements (series of spring and dashpot) in parallel. If an additional equilibrium network (spring) is used (Fig. 13.1), the material model will represent a solid behavior [21]. In this case, the stress in a stress relaxation experiment would relax to a non zero plateau, which is defined by the stress in the equilibrium network. Without the equilibrium network, the stress would relax to zero, which

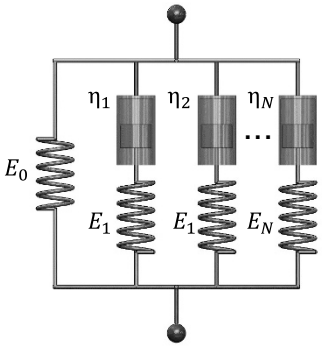

Fig. 13.1 Illustration of the generalized Maxwell solid model which consists of a series of Maxwell elements in parallel and one equilibrium network.

represents a fluid-like behavior [21]. Rheological models, such as the generalized Maxwell model are often used as a starting point for the development of nonlinear viscoelastic models [19]. In Subsect. 13.4.2, the setup of the generalized Maxwell model is used to develop a simplified one-dimensional model which represents the nonlinear viscoelastic PRF model.

13.2.2 Abaqus Parallel Rheological Framework Model

Similar to the generalized Maxwell model (Fig. 13.1), the Abaqus PRF model consists of an arbitrary number of viscoelastic networks in parallel and an optional equilibrium network [17]. The main difference to the generalized Maxwell model is that nonlinear hyperelastic models are used for the springs and nonlinear creep laws for the dashpots. The response of the equilibrium network can be purely elastic or elastoplastic [17]. For each viscoelastic network $i = 1, 2, 3, \ldots, N$, a multiplicative split of the deformation gradient into an elastic and an inelastic part is assumed [17]

$$\boldsymbol{F} = \boldsymbol{F}^{\text{el}} \cdot \boldsymbol{F}^{\text{in}}. \tag{13.9}$$

The elastic response of the PRF model can be represented by any hyperelastic model implemented in Abaqus [18]. Similar to the Prony values g_i of the linear viscoelastic model, the stiffness of each network is represented by a stiffness ratio s_i where the sum of all stiffness ratios must be less or equal to one. In case the stiffness ratio is equal to one, the model is defined without equilibrium network. The same hyperelastic model is used for all networks. Using Abaqus, all hyperelastic models are described by an energy potential $U(\varepsilon)$ as a function of the strain [18].

Considering the shrinkage and warpage analysis, the strains are rather small so that a linear elastic model would do well. Thus a simple Neo-Hookean hyperelastic model is used in this study. The strain energy potential is given by [18]:

$$U = C_{10}\,(\bar{I}_1 - 3) + \frac{1}{D_1}(J^{\text{el}} - 1)^2. \tag{13.10}$$

Thereby C_{10} and D_1 are material parameters, $\bar{I}_1$ is the first deviatoric strain invariant and J^{el} is the elastic volume ratio. The viscous behavior for each network is defined using the creep potential G^{in} [18]. The creep potential is given by the equivalent deviatoric Cauchy stress $\bar{p}$, so that the flow rule can be described as follows [18]:

$$\boldsymbol{D}^{\mathrm{in}} = \frac{3}{2\,\tilde{q}}\,\dot{\bar{\varepsilon}}^{\mathrm{in}}\,\bar{\boldsymbol{\tau}}, \tag{13.11}$$

with

$$\tilde{q} = J\,\bar{p}, \tag{13.12}$$

where $\boldsymbol{D}^{\mathrm{in}}$ is the symmetric part of the velocity gradient $\boldsymbol{L}^{\mathrm{in}}$, $\bar{\boldsymbol{\tau}}$ is the deviatoric Kirchhoff stress, J is the determinant of the deformation gradient $\boldsymbol{F}$, the so called Jacobien, and $\dot{\bar{\varepsilon}}^{\mathrm{in}}$ the equivalent creep strain rate. For the evolution of the creep strain rate, several models are available in Abaqus. These are the power law model, the strain hardening model, the hyperbolic-sine model, the Bergstrom-Boyce model, and a user-defined creep model which can be implemented by a user subroutine [18]. In this study, the strain hardening model (Eq. (13.13)) is used for the evaluation of the creep strain rate [18]

$$\dot{\bar{\varepsilon}}^{\mathrm{in}} = \left(A\,\tilde{q}^{n}\,[(m+1)\,\bar{\varepsilon}^{\mathrm{in}}]^{m}\right)^{\frac{1}{m+1}}, \tag{13.13}$$

where $\bar{\varepsilon}^{\mathrm{in}}$ is the equivalent inelastic strain and A, m and n are material parameters. If parameter n is set equal to one and m is set equal to zero, the evolution of the creep strain rate $\dot{\bar{\varepsilon}}^{\mathrm{in}}$ is linearized [17].

Similar to the linear viscoelastic model, the reduced time concept can be used to model temperature effects [18]. In contrast to the linear viscoelastic model where the same WLF or Arrhenius parameters are used for all networks, the PRF model allows the specification for each network individually. Alternatively, all parts of the material model, the instantaneous modulus, the creep model, and the stiffness ratios s_i can be defined temperature-dependently using tabular values [18]. For temperatures between the specified temperatures, the material parameters are interpolated. In the shrinkage and warpage analysis, the temperature changes continuously from a high temperature to room temperature (RT). Therefore, the reduced time concept is used in this study to realize a continuous function for the temperature dependence of the material model.

Currently [18], only isotropic thermal expansion can be used with the Abaqus PRF model. This excludes the use of orthotropic process-dependent expansion coefficients as they were used in [8].

13.3 Shrinkage and Warpage Analysis

The simulation workflow for the shrinkage and warpage analysis of extrusion blow molded parts has been described in detail in [8], so that we will only recall the most important parts for this study. Considering a complex extrusion blow molded part, at

least three simulation steps are necessary for the shrinkage and warpage prediction. The first step is the process simulation of the parison inflation to determine the process-related wall thickness distribution. After the process simulation, the cooling of the part inside the closed mold and at ambient air after demolding is analyzed. The transient temperature field is then used in a subsequent shrinkage and warpage analysis to determine the part deformation. For the process simulation, currently B-SIM of Accuform, a finite element based process simulation software for blow molding applications, is used. The resulting wall thickness distribution as well as local degrees of stretching and their orientation are mapped to the finite element mesh of the following analysis steps using the MpCCI Mapper of Fraunhofer SCAI. Since blow molded parts are thin-walled components, shell elements are used for the cooling and warpage analysis. The part cooling is analyzed in two steps using Simulia Abaqus (Dassault Systèms). In the first step, the part cools down under mold constraint. Due to the contact with the cooled mold, the outer surface cools down rapidly whereas the inner surface cools down much slower. After demolding, further cooling takes place at ambient air until RT is reached. Similarly to the cooling simulation, the shrinkage and warpage analysis is also carried out in two steps using Abaqus. In the first step, all degrees of freedom of all nodes are fixed so that thermal stresses will build up during the cooling under mold constraint. In the second step, the boundary conditions are changed so that the part can shrink and warp freely due to the accumulated thermal stresses and further temperature changes at ambient air.

In this study, we will focus on a one-element simulation of the shrinkage analysis which sufficiently represents a local area of a complex blow molded part. The cooling simulation will be carried out using the simulation model published in [8]. A wall thickness of 2 mm and a cooling time of 60 s is used. The required temperature-dependent material data for density, thermal conductivity, and heat capacity as well as the heat transfer coefficients are taken from [8, 22, 23]. For the shrinkage and warpage analysis, the thermal expansion behavior and the mechanical material behavior need to be defined. Because the thermal expansion behavior of HDPE is highly temperature-dependent, a temperature-dependent CTE is taken from literature [22, 23] (Fig. 13.2). The CTE was determined from Pressure-Volume-Temperature (P-V-T) data at a pressure of approximately 0.1 N/mm^2 [22, 23]. The peak at 130 °C marks the crystallite melting temperature where the volume of the polymer drastically changes.

For the definition of the mechanical behavior, a master curve was obtained from dynamic mechanical analysis (DMA) using frequency sweeps in the temperature range of −20 – 120 °C [8]. The WLF equation was used to shift the isothermals of the temperature-frequency-sweeps with RT as θ_{Ref} to obtain a continuous master curve at RT. The storage modulus E' was then converted from the frequency domain to the time domain using the following approximation formula [24, 25]:

$$t = \frac{1}{2\pi f}. \tag{13.14}$$

Considering the part cooling, a large temperature range from about 200 °C to RT needs to be considered. After demolding, a viscoelastic retardation occurs, due to

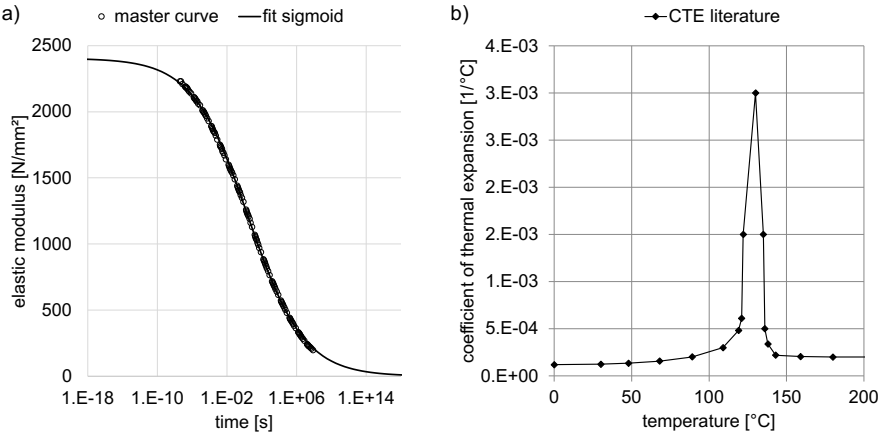

Fig. 13.2: Material data for the shrinkage and warpage analysis. a) Experimental master curve obtained from DMA experiments [8]. The master curve is fitted by a sigmoid function and extrapolated to cover the whole time range; b) Temperature-dependent CTE [22, 23].

the accumulated thermal stresses [26]. This retardation can take several hours to days. To cover the extensive time and temperature range in the material modeling, the experimental master curve is extrapolated. Due to the typical s-formed shape, a sigmoid function is used to fit and extrapolate the experimental data. The extrapolated master curve is given by Eq. (13.15) (Fig. 13.2)

$$f(t) = -1201.79 \tanh\left(\frac{\log_{10}(t) - 0.449}{6.37}\right) + 1201.79. \tag{13.15}$$

Using one relaxation time per decade, the linear viscoelastic model is calibrated using Eq. (13.3) with 37 prony terms (Fig. 13.3). The same relaxation function is used for the normalized shear and bulk relaxation function $g_R(t)$ and $\kappa_R(t)$. The Poissons ratio is set to 0.5, so that incompressibility is assumed. For the temperature dependence of the material model, the reduced time concept is applied, using the WLF equation for the approximation of the shift function. The WLF coefficients of the master curve creation are used in the simulation model.

At the crystallite melting temperature T_m, the material behavior changes from a thermo-viscoelastic solid to a thermo-viscoelastic fluid with a structural stiffness of almost zero. It is therefore assumed that the evolution of thermal stresses in the shrinkage analysis starts at temperatures below 130 °C. To ensure that no thermal stress is stored in the material model at temperatures above 130 °C, the CTE is set to zero (Fig. 13.3). Since the demolding temperatures are usually below 130 °C, free shrinkage at temperatures above 130 °C can be ruled out.

If the nonlinear viscoelastic PRF model is used with the reduced time concept to model temperature effects, the short relaxation times will cause convergence problems at high temperatures. This is because the already short relaxation times will be further

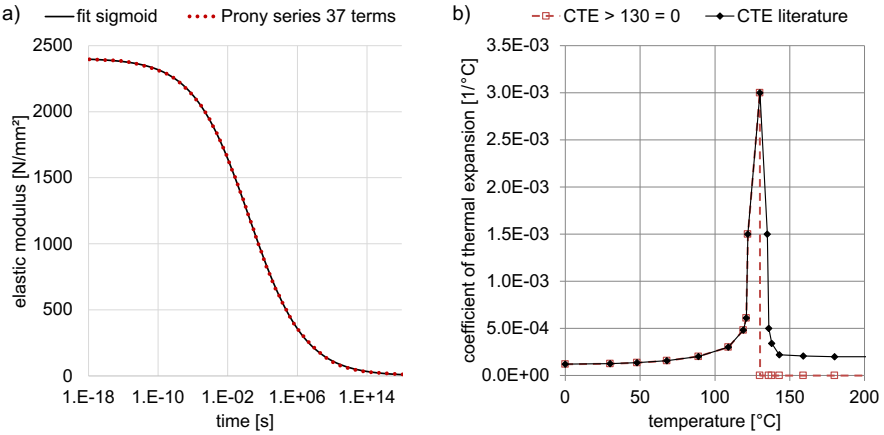

Fig. 13.3: Material data for the shrinkage and warpage analysis. a) Experimental master curve obtained from DMA experiments [8] which is extrapolated using a sigmoid function. A Prony series is used to fit a linear viscoelastic material model (generalized Maxwell solid model) to the sigmoid function; b) Temperature-dependent CTE according to [22, 23], and modified CTE which is set to zero for temperatures which are above the crystallite melting temperature.

shortened by the use of the WLF or Arrhenius equation. However, in a shrinkage and warpage analysis, high strain rates will only occur at very high temperatures at the outer surface where the cooling rate is high. Below 130 °C, the cooling rate is much lower. For the use of the PRF model, the short time behavior between 10^{-18} and 1.0 s is neglected. The prony series is then modeled at RT with an instantaneous modulus of 1450 N/mm^2 and the first relaxation time is set to 1.0 s. 19 Prony terms are used to model the material behavior in the range 1.0 s until 10^{18} s. To validate this approach, a shrinkage analysis using a linearized version of the PRF model with 19 networks is carried out and compared to a shrinkage analysis using the linear viscoelastic model with 19 and 37 networks respectively.

For small strains, the response of the Neo-Hookean model will be similar to a linear elastic model. At these small strains, the nonlinear behavior of the PRF model results mainly from the viscous flow which is modeled by the strain hardening model (Eq. (13.13)). To obtain a linear viscoelastic representation of the PRF model, the strain hardening model needs be converted to linear flow. This can be achieved by setting the n-parameter of each viscoelastic network i equal to one and the m-parameter equal to zero. The parameter A_i for each network can then be calculated using the instantaneous elastic modulus E, the Prony values g_i, and relaxation times τ_i of each network of the linear viscoelastic model as follows:

$$A_i = \frac{1}{E\, g_i\, \tau_i}. \tag{13.16}$$

For the elastic part of the PRF model, the parameter D_1 of the Neo-Hookean model (Eq. (13.10)) is set to zero to obtain incompressibility. The parameter C_{10} can

then be determined using the instantaneous elastic modulus and the Poissons ratio of the linear viscoelastic model (Eq. (13.17)). The stiffness ratios will be equal to the Prony values of the linear model ($s_i = g_i$).

$$C_{10} = \frac{E}{2\,[2\,(1+\nu)]} = \frac{E}{6}. \tag{13.17}$$

The results of the two linear viscoelastic models with 37 and 19 prony terms are compared to the linearized PRF model in Fig. 13.4. Fig. 13.4a shows the thermal stress accumulated during the cooling under mold constraint. The stress at the outer surface is much higher due to the higher cooling rate. Fig. 13.4b shows the viscoelastic retardation for a period of 24 h after demolding. The response of the linear viscoelastic model is exactly the same if the prony series is reduced from 37 to 19 terms. The linearized PRF model deviates slightly from the linear viscoelastic representation (Fig. 13.4). However, since the differences are quite small, numerical reasons are suspected.

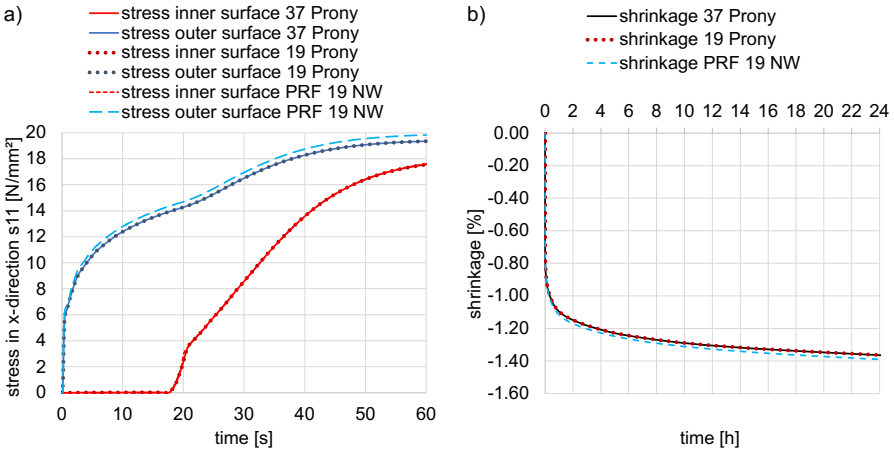

Fig. 13.4: Comparison of a one-element shrinkage analysis using a linear viscoelastic model with 37 Prony terms, a linear viscoelastic model with 19 Prony terms and a linearized PRF model with 19 networks (NW). a) Build up of thermal stresses of the inner and outer surface during cooling under mold constraint; b) Shrinkage for a period of 24 h after demolding.

13.4 Calibration Strategy

Due to the complexity of the PRF model, an elaborate calibration strategy is needed to find suitable material parameters to match a set of experimental measurement data. Using the strain hardening model, each network is described by the four material

parameters s_i, A_i, n_i and m_i. In addition, the modulus of the entire network and the activation energy of the Arrhenius equation also have to be determined. Even if only three networks are used, the total amount of parameters to be identified is 14. For six networks 26 parameters and for 12 networks 50 material parameter need to be identified. It can be expected that for a nonlinear viscoelastic model, less networks are needed compared to the linear viscoelastic model. However, considering a large time and temperature range to cover, several networks might be necessary for an accurate representation of the experimental data. This involves the determination of a large set of material parameters. The associated objective function of the optimization problem to solve might have many local minima. To find the best possible solution, the use of global optimization methods is necessary.

In the following, a calibration strategy is presented, which uses functional relations to describe the material parameters of the individual networks. Thus, the dimension of the design space is reduced to a manageable number. However, the use of a global optimization strategy is still associated with high computational effort if a large number of optimization loops is involved. In each optimization loop, a numerical model of the experiment is computed and the results are compared to the measurement data. The most expensive part is the numerical simulation of the material test. If a finite element analysis using Abaqus is carried out, even if just one element is used, several seconds are needed for the verification of license and the interpretation of the input deck. To save computation time, a simplified numerical model which represents the PRF model is implemented in Matlab. In the following, the material data for the model calibration as well as the reduction of the material parameters and the computation time is explained in detail.

13.4.1 Experimental Data

The shrinkage and warpage analysis can be divided into a loading phase in which thermal stresses will build up and relax during the cooling under mold constraint, followed by an unloading (demolding) where the part is free to shrink. For the model calibration, a set of experiments is used which involves a loading and relaxation phase followed by an unloading phase. Therefore, relaxation tests with subsequent unloading at several temperature and strain levels are carried out using a Zwick Kappa Multistation. Material samples of type 1A (DIN EN ISO 527-2) of the blow molding HDPE grade Lupolen 5021DX (LyondellBasell) were taken from compression molded plates (polystat 200 T/2, Servitec, at 210 °C and 200 bar ($2\ 10^7$ Pa) for 70 s) with 2 mm thickness. At RT, three different strain levels (0.5 %, 1.0 % and 2.0 %) were investigated. The highest strain level was also tested at different temperatures (RT, 40 °C, 60 °C, 80 °C and 100 °C). For each test point, the average of three measurements is taken. At the beginning of the loading phase, a constant strain rate of $0.0015\,s^{-1}$ was applied to the sample until the specified strain level was reached. The strain level was then held constant (strain controlled) for a period of 600 s to measure the stress relaxation response. At the end of the loading phase, the sample was unloaded (force

controlled) with a force rate of 300 N/s. The force was then held constant at zero N for a period of 1800 s to measure the viscoelastic retardation. Fig. 13.5 shows the measured stresses and strains of the relaxation tests with subsequent unloading.

13.4.2 Implementation of a One-Dimensional Model to Reduce Computation Time

To develop an efficient numerical model which represents the PRF equations of a relaxation test with subsequent unloading, four steps are considered. The first step covers the loading, assuming a constant strain rate. Once the final strain is reached, it is held constant over a defined period of time. The third step covers the unloading, assuming a constant stress rate. Once the stress approaches zero, it is held at zero for a defined period. The Matlab implementation will be a one-dimensional representation of the material equations of the PRF model. In contrast to the Abaqus model, only the material equations are solved, so that no spatial discretization is needed. This reduces the system of partial differential equations (PDE) to a system of ordinary

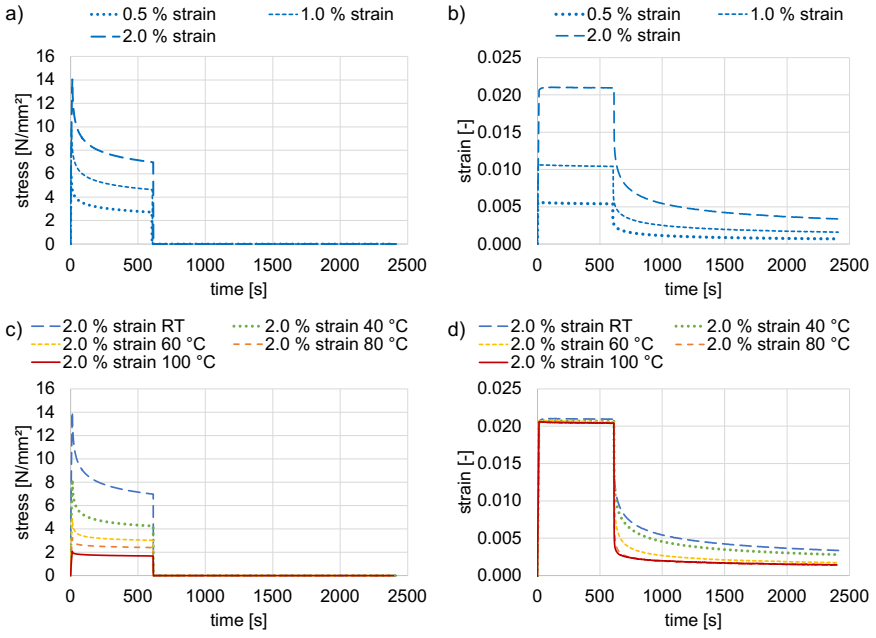

Fig. 13.5: Experimental data of a stress relaxation test with subsequent unloading for different strain and temperature levels. a) Stresses for three different strain levels at RT; b) Strains of the experiments for three different strain levels at RT; c) Stresses of a strain level of 2.0 % at different temperatures; d) Strains of a strain level of 2.0 % at different temperatures.

differential equations (ODE) which can be efficiently solved using a suitable ODE solver.

For the model we start with the total stress σ_{total} of the framework, which is the sum of all network stresses σ_i

$$\sigma_{\text{total}} = \sigma_0 + \sum_{i=1}^{N} \sigma_i. \tag{13.18}$$

The total strain is equivalent in each network element due to the parallel arrangement (Fig. 13.1) and is decomposed additively into an elastic part (spring) and an inelastic part (dashpot)

$$\varepsilon_{\text{total}} = \varepsilon_i^{\text{el}} + \varepsilon_i^{\text{in}}. \tag{13.19}$$

Since the strains in the performed material tests are small, it can be assumed that a linear elastic material model is sufficient for the description of the springs. The stress of each network is then calculated by Hooke's law:

$$\sigma_i = \varepsilon_i^{\text{el}} E_i, \tag{13.20}$$

where E_i is the elastic modulus of the i'th network. For the stress of the equilibrium network applies:

$$\sigma_0 = \varepsilon_{\text{total}} E_0. \tag{13.21}$$

The strain rate of the dashpots is represented by the strain hardening model.

$$\dot{\varepsilon_i}^{\text{in}} = \left(A_i \, \sigma_i^{n_i} \, [(m_i + 1) \, \varepsilon_i^{\text{in}}]^{m_i} \right)^{\frac{1}{m_i+1}}, \tag{13.22}$$

where $\dot{\varepsilon}_i$ is the inelastic strain rate of the network, and A_i, n_i and m_i are material parameters. By taking the time derivative of Eq. (13.19) and (13.20), we obtain:

$$\dot{\varepsilon}_{\text{total}} = \dot{\varepsilon}_i^{\text{el}} + \dot{\varepsilon}_i^{\text{in}}, \tag{13.23}$$

and

$$\dot{\sigma}_i = \dot{\varepsilon}_i^{\text{el}} E_i. \tag{13.24}$$

Substituting Eq. (13.22) and Eq. (13.24) into Eq. (13.23) and rearranging gives an ordinary differential equation of the form $f(t, \sigma_i, \dot{\sigma_i}) = 0$ for the i'th network

$$\dot{\sigma}_i = \dot{\varepsilon}_{\text{total}} E_i - E_i \left(A_i \, \sigma_i^{n_i} \, [(m_i + 1) \, \varepsilon_i^{\text{in}}]^{m_i} \right)^{\frac{1}{m_i+1}}. \tag{13.25}$$

Equation (13.25) still contains the unknown inelastic strain $\varepsilon_i^{\text{in}}$. By replacing $\varepsilon_i^{\text{in}}$ by the expression $\varepsilon_{\text{total}} - \frac{\sigma_i}{E_i}$, a differential equation is obtained which contains only known quantities

$$\dot{\sigma}_i = \dot{\varepsilon}_{\text{total}} E_i - E_i \left(A_i \, \sigma_i^{n_i} \left[(m_i + 1) \left(\varepsilon_{\text{total}} - \frac{\sigma_i}{E_i} \right) \right]^{m_i} \right)^{\frac{1}{m_i+1}}. \tag{13.26}$$

To model the temperature dependency of the material model, the inelastic strain rate of each network is divided by the shift factor $\alpha(T)$

$$\dot{\sigma}_i = \dot{\varepsilon}_{\text{total}} E_i - \frac{E_i \left(A_i \, \sigma_i^{n_i} \left[(m_i + 1) \left(\varepsilon_{\text{total}} - \frac{\sigma_i}{E_i} \right) \right]^{m_i} \right)^{\frac{1}{m_i+1}}}{\alpha(T)}. \tag{13.27}$$

The shift factor is calculated using the Arrhenius equation (Eq. (13.8)). The stresses σ_i of the N individual networks are obtained by solving Eq. (13.27) with an ODE solver. The Matlab solver ode15s turned out to be very efficient for this kind of problem.

Depending on the choice of the parameters m_i and n_i, numerical difficulties can occur if the network stress σ_i is negative. This can in some cases lead to complex numbers. In order to deal with these difficulties, Eq. (13.27) is modified as follows:

$$\dot{\sigma}_i = \dot{\varepsilon}_{\text{total}} E_i - \frac{\sigma_i}{|\sigma_i|} \frac{E_i \left(A_i \, |\sigma_i|^{n_i} \left[(m_i + 1) \left| \varepsilon_{\text{total}} - \frac{\sigma_i}{E_i} \right| \right]^{m_i} \right)^{\frac{1}{m_i+1}}}{\alpha(T)}. \tag{13.28}$$

By taking absolute values of σ_i and $\varepsilon_{\text{total}} - \frac{\sigma_i}{E_i}$, complex numbers are ruled out. The term $\frac{\sigma_i}{|\sigma_i|}$ is introduced to define the direction of the viscous flow.

For the unloading phase and the subsequent holding phase, the external stress rate respectively the external stress (which is zero) is specified but the internal network stresses and stress rates are unknown. Therefore, instead of the equation for the entire system, the differential equations of the dashpots are considered (Eq. (13.22)). The unknown network stress σ_i is replaced by the expression $E_i(\varepsilon_{\text{total}} - \varepsilon_i^{\text{in}})$. One obtains:

$$\dot{\varepsilon}_i^{\,\text{in}} = \frac{(E_i(\varepsilon_{\text{total}} - \varepsilon_i^{\text{in}}))}{|E_i(\varepsilon_{\text{total}} - \varepsilon_i^{\text{in}})|} \frac{\left(A_i \, |E_i(\varepsilon_{\text{total}} - \varepsilon_i^{\text{in}})|^{n_i} [(m_i + 1)|\varepsilon_i^{\text{in}}|]^{m_i} \right)^{\frac{1}{m_i+1}}}{\alpha(T)}. \tag{13.29}$$

To solve this ODE, it is necessary to replace the total strain with known quantities. For the equilibrium network applies:

$$\sigma_0 = \sigma_{\text{total}} - \sum_{i=1}^{N} (\varepsilon_{\text{total}} E_i - \varepsilon_i^{\text{in}} E_i). \tag{13.30}$$

If we substitute this expression into Eq. (13.21) and rearrange, we get the following equation:

$$\varepsilon_{\text{total}} = \frac{\frac{\sigma_{\text{total}}}{E_0} + \sum_{i=1}^{N} \varepsilon_i^{\text{in}} \frac{E_i}{E_0}}{1 + \sum_{i=1}^{N} \frac{E_i}{E_0}}. \tag{13.31}$$

By substituting $\varepsilon_{\text{total}}$ in Eq. (13.29) by Eq. (13.31), the inelastic strain of the i'th network can be computed using the elastic moduli and inelastic strains of all N networks. The system of coupled differential equations is also solved with the Matlab solver ode15s.

So far, the moduli of the individual networks are specified directly. Alternatively, stiffness ratios as used by Abaqus can be specified to define the stiffness of each network. In this case, the total elastic modulus E_{total} of all networks and a stiffness ratio s_i for each network will be specified. The moduli E_i of each network is then calculated by the following equations:

$$E_i = s_i \, E_{\text{total}}. \tag{13.32}$$

For the modulus of the equilibrium network applies:

$$E_0 = E_{\text{total}} - \sum_{i=1}^{N} s_i \, E_{\text{total}}. \tag{13.33}$$

13.4.3 Reduction of Material Parameters

To reduce the amount of parameters in the model calibration, we start with the prony fit of the linear viscoelastic model to the extrapolated sigmoid curve. The sigmoid curve was fitted by the prony series using one relaxation time τ per decade. If we plot the Prony values over the network number, they can be approximated by a normalized Gaussian function (Eq. (13.34), Fig. 13.6)

$$s_i = \frac{1}{12.9} \, \mathrm{e}^{\left(-\frac{1}{2}\left(\frac{i-19.8}{5.15}\right)^2\right)}. \tag{13.34}$$

Using the Gauss function for the description of the stiffness ratio of each network "i", a normalization is needed to ensure that the sum of all stiffness ratios is always smaller or equal to one. We start with the Gauss function without normalization. The parameters p_{s1} and p_{s2} are used to modify the distribution of the stiffness ratios s_i

$$s_i = \mathrm{e}^{\left(-\frac{1}{2}\left(\frac{i-p_{s1}}{p_{s2}}\right)^2\right)}. \tag{13.35}$$

The parameter p_{s1} is used to shift the Gauss function on the abscissa. Parameter p_{s2} can be used to change the curvature. In the next step, the sum of the stiffness ratios of all networks is calculated

$$s_{\text{sum}} = \sum_{i=1}^{N} s_i. \tag{13.36}$$

The normalized Gauss function is obtained as follows:

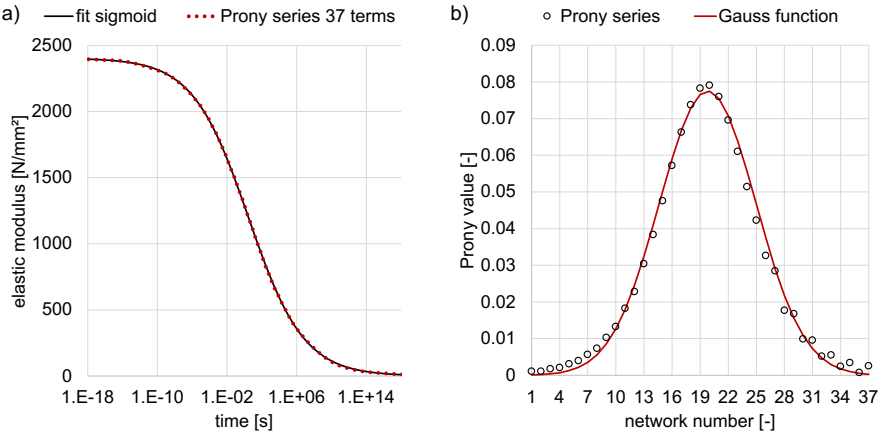

Fig. 13.6: Approximation of the Prony values by a Gauss function. a) Extrapolated master curve which is approximated using a Prony series with 37 terms; b) Distribution of the Prony values with respect to the network number. The Prony values are approximated using a Gaussian function.

$$s_{i_{\text{norm}}} = \frac{p_{\text{s3}}}{s_{\text{sum}}} \mathrm{e}^{\left(-\frac{1}{2}\left(\frac{i-p_{\text{s1}}}{p_{\text{s2}}}\right)^2\right)}. \tag{13.37}$$

Using the parameter p_{s3}, the sum of the stiffness ratios can be modified to obtain values less than one. Thus, the stiffness ratio of an arbitrary number of networks is described by just three parameters. Also the sum of the stiffness ratios is always less or equal to one, so that no restrictions are necessary within the optimization. As presented in Sect. 13.3, the short-time behavior of the master curve will be neglected to overcome convergence problems at higher temperatures. The first relaxation time τ_i is set to 1.0 s, so that 19 networks are used in total. Therefore, the Gauss function is shifted using parameter p_{s1}.

The relaxation times τ_i of the prony series are held constant to ensure that the distribution of the stiffness ratios follows Eq. (13.37). For the PRF model, we assume that the A-values can be calculated by Eq. (13.16) using the stiffness $s_i E$ and the relaxation time τ_i. For the linearized PRF model ($n_i = 1$ and $m_i = 0$), the inelastic strain rate of the strain hardening model (Eq. (13.22)) is proportional to the stress σ_i. However, for $n > 1$ and $m < 0$ the strain hardening law becomes nonlinear. As the network stress σ_i is raised to the power of n_i ,the inelastic strain rate increases nonlinearly with increasing stress. At stresses below $1\,\text{N/mm}^2$ the strain rate will be even slower compared to a linearized model and it drastically increases for higher n-values if the stress increases. If higher stresses are involved it might be necessary to adjust the A-values of the networks. However, the stresses for the investigated HDPE are rather moderate (less than $15\,\text{N/mm}^2$, Fig. 13.5). Using 19 networks, the individual network stress σ_i will be close to one for most networks. In this case, the inelastic strain rate will be a nonlinear function of the applied stress but it won't differ too much from the strain rate of the linearized model. Therefore, it seems reasonable

to use constant relaxation times τ of the linear model to calculate the A-values of the PRF-model via Eq. (13.16). The A-values are thus excluded from the design space of the parameter optimization.

Similarly to the stiffness ratios, n- and m-parameters of all networks will also be described using a suitable functional relation. In order to ensure stability of the model over the entire time and temperature range, the following boundaries are set:

$$1.0 \leq n_i \leq 5.0, \tag{13.38}$$

$$-0.7 \leq m_i \leq 0.0. \tag{13.39}$$

In contrast to the stiffness ratios, a suitable distribution of the n- and m-parameters with respect to the network number is unknown. However, it is assumed that the individual n- and m-parameters can be represented by a monotonically increasing or decreasing function. A sigmoid function using four parameters is used for the distribution. Depending on the parameter selection, the sigmoid function can describe an s-curve, a curve or even a constant (Eq. (13.40), (13.41)). Some possible distributions for the parameters s, n, and m are shown in Fig. 13.7.

$$n_i = p_{\mathrm{n1}} + ((p_{\mathrm{n1}} - 1)\, p_{\mathrm{n2}}) \tanh\left(\frac{i - p_{\mathrm{n3}}}{p_{\mathrm{n4}}}\right), \tag{13.40}$$

$$m_i = p_{\mathrm{m1}} + (p_{\mathrm{m1}}\, p_{\mathrm{m2}}) \tanh\left(\frac{i - p_{\mathrm{m3}}}{p_{\mathrm{m4}}}\right). \tag{13.41}$$

Using the described Gauss and sigmoid functions, the design space for the model calibration is reduced to 11 parameters independent of the amount of networks.

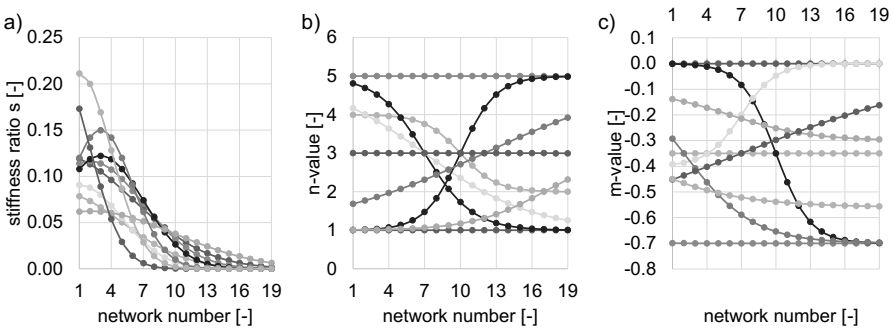

Fig. 13.7: Distribution of the material parameters of the individual networks. The curves show different possible distributions based on the three parameter Gauss function and the four parameter sigmoid functions. a) Example distributions of stiffness ratios s_i using a three parameter description of a Gaussian function; b) Example distributions of the n-values using a four parameter sigmoid function; c) Example distributions of the m-values using a four parameter sigmoid function.

13.4.4 Calibration Workflow

For the calibration of the PRF model, the process automation and design exploration software tool Simulia Isight (Dassault Systèmes) is used. The complete optimization workflow is illustrated in Fig. 13.8.

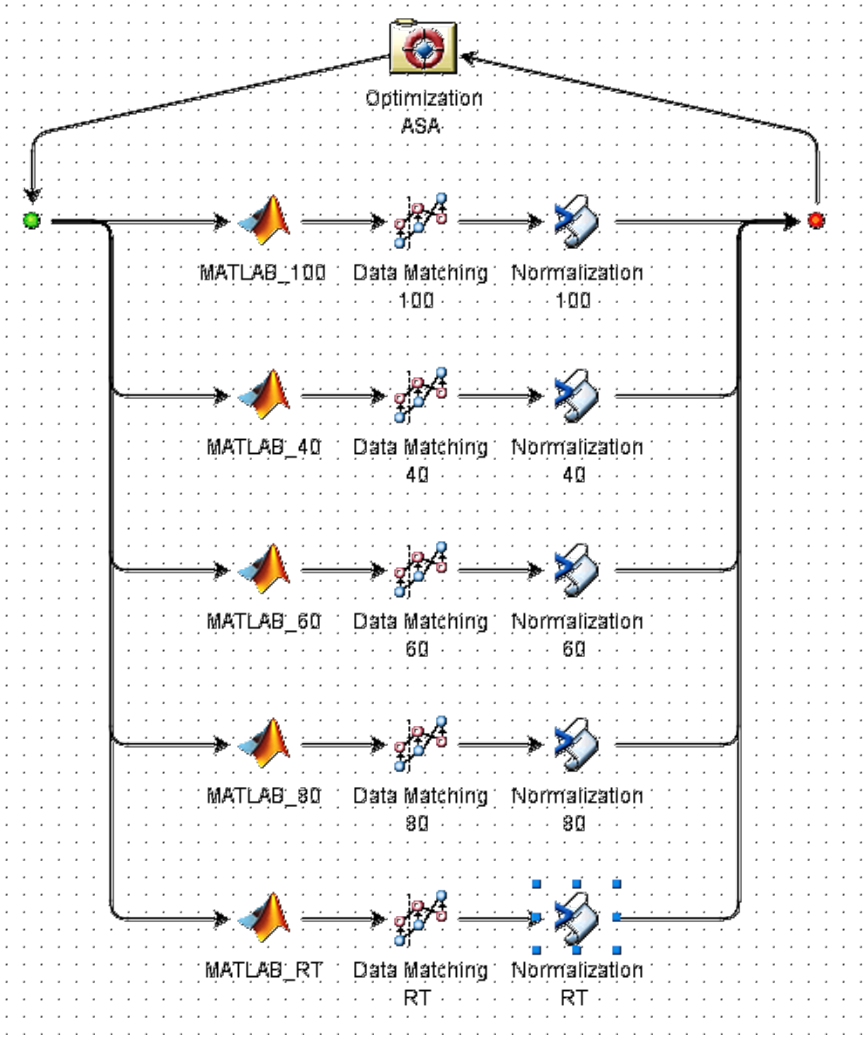

Fig. 13.8: Optimization workflow using the process automation and design exploration software Simulia Isight.

The global optimization algorithm Adaptive Simulated Annealing is used with a total amount of 10,000 design loops. This algorithm is well suited for the search of a global optimum especially for highly nonlinear problems with short calculation times [18]. In each design loop of the optimization, a Matlab component is executed which runs a numerical model of the experimental test. The Matlab model which represents the material tests at RT is used to simulate all three strain levels. All testing temperatures run in parallel, so that all 10,000 runs are calculated in less than three hours on a personal computer.

The data matching components are used for the calculation of the sum of the absolute difference between points on the simulated curves and the experimental curves. The simulation data is therefore interpolated to the measurement data. The error of the loading and unloading phase is calculated separately. After the error calculation, a script component is used to normalize the data to obtain an error value in percent. This is necessary in order to achieve equal weighting to loading and unloading. Thus the error of each virtual experiment phase is calculated as follows:

$$\mathrm{Err} = \frac{\sum_{j=1}^{N} |Y_{j_{\mathrm{exp}}} - Y_{j_{\mathrm{sim}}}|}{\sum_{j=1}^{N} Y_{j_{\mathrm{exp}}}} \cdot 100\,\%, \tag{13.42}$$

where Err is the error value in %, $Y_{j_{\mathrm{exp}}}$ is the experimental value at data point j, and $Y_{j_{\mathrm{sim}}}$ is the simulated value at data point j. To obtain the total error of all experiments, the average of all error values is calculated.

The calibration workflow using the Gauss and sigmoid functions for the parameter reduction is tested and compared to an optimization where the parameters are varied freely between boundaries. Using the free parameter variation, the stiffness of the networks is specified directly by the elastic modulus of the network to avoid violation of the condition that the sum of all stiffness ratios must be less or equal to one. The parameters as well as their boundaries of the free parameter variations are given by Table 13.1. For all model calibrations, the Arrhenius function using the same activation energy E_{A} for all networks is used. For the calibration model which uses the Gauss and sigmoid functions to describe the parameters s_i, n_i, and m_i, the elastic modulus of the whole network E_{total} is also used as a parameter in the calibration process. The lower boundary is set to $1{,}000\,\mathrm{N/mm^2}$ and the upper boundary is set to $2{,}000\,\mathrm{N/mm^2}$. The free optimization is tested with different numbers of networks, that is to say three, six and 12. Table 13.2 gives an overview over the different models which are used in the calibration process.

13.5 Results

Using the model variations shown in Table 13.2 the PRF model was calibrated using the experimental measurement data illustrated in Fig. 13.5. The overall errors

Table 13.1: Boundaries of the free parameter variations.

Parameter	lower bound	upper bound
E_0	$1\,\frac{\mathrm{N}}{\mathrm{mm}^2}$	$700\,\frac{\mathrm{N}}{\mathrm{mm}^2}$
E_i	$1\,\frac{\mathrm{N}}{\mathrm{mm}^2}$	$700\,\frac{\mathrm{N}}{\mathrm{mm}^2}$
A_i	$10^{-15}\left(\frac{\mathrm{N}}{\mathrm{mm}^2}\right)^{-n}\,\mathrm{s}^{-m-1}$	$10^{-3}\left(\frac{\mathrm{N}}{\mathrm{mm}^2}\right)^{-n}\,\mathrm{s}^{-m-1}$
m_i	-0.7	0.0
n_i	1.0	5.0
EA	$100,000\,\frac{\mathrm{J}}{\mathrm{mol}}$	$300,000\,\frac{\mathrm{J}}{\mathrm{mol}}$

Table 13.2: Model variations which are tested in the model calibration.

NW	Model	Parameter Variation	Parameter Amount
3	PRF	free	14
6	PRF	free	26
12	PRF	free	50
19	PRF	function	13

of the model calibrations are shown in Table 13.3. Comparing the results of the free parameter variation with the use of functional relations between the individual network parameters, it can be seen that the latter approach achieves the best results with an error of about 5.9 % (Table 13.3). The poorest result is obtained by the PRF model with just three networks, with an error of 20.3 %. Doubling the number of networks from three to six halves the error. A further duplication from six to 12 networks leads to slightly poorer results.

Figure 13.9 shows the distribution of s_i, n_i, and m_i of the best design point. It is clearly visible that the stiffness ratios become zero after the ninth network. In this case the amount of networks can be reduced to nine. The results are identical to the results using 19 networks. The n-values show a monotonically increasing trend, whereas the m-values lie on a decreasing s-curve.

Figure 13.10 shows a comparison between the results of the Matlab models and Abaqus finite element simulations for the best design point. The results are in very good agreement. Only at the highest strain level, a negligible deviation in the unloading phase can be observed.

Table 13.3: Representation of the error value of the free model calibration using three, six and 12 networks compared to the error of the model calibration using functional relations between the network parameters.

NW	Model	Parameter Variation	Parameter Amount	Error
3	PRF	free	14	20.3 %
6	PRF	free	26	10.8 %
12	PRF	free	50	11.5 %
19	PRF	function	13	5.9 %

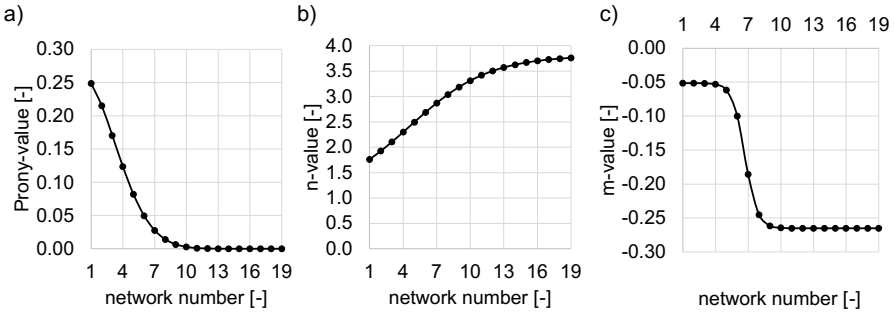

Fig. 13.9: Distribution of the material parameters of the individual networks for the best design point. a) Distributions of the stiffness ratios s_i using the three parameter description of the Gaussian function; b) Distributions of the n-values using the four parameter sigmoid function; c) Distributions of the m-values using the four parameter sigmoid function.

Comparing the Abaqus results of the best design point to the experimental data, a good agreement is observed (Fig. 13.11). The stress relaxation curve at 2 % and 100 °C with an error of 24 %, the stress relaxation curve at 2 % strain at RT with 19 % error, and the unloading curve at 2 % strain and 80 °C with an error of about 13 % show the largest deviation. All other curves are in good agreement with the experimental data.

In Fig. 13.12, the PRF model using the parameters of the best design point is integrated in the shrinkage model and the results are compared to the results of the linear viscoelastic model which was calibrated using the master curve. The stress history of the PRF model during the cooling under mold constraint is similar to the linear viscoelastic model. However, the stresses of the PRF model are a slightly lower than the stresses of the linear viscoelastic model. Moreover, the difference in stress between the inner surface and the outer surface is smaller for the PRF model. Comparing the shrinkage behavior in the first 24 h, the PRF model shows a stronger retardation.

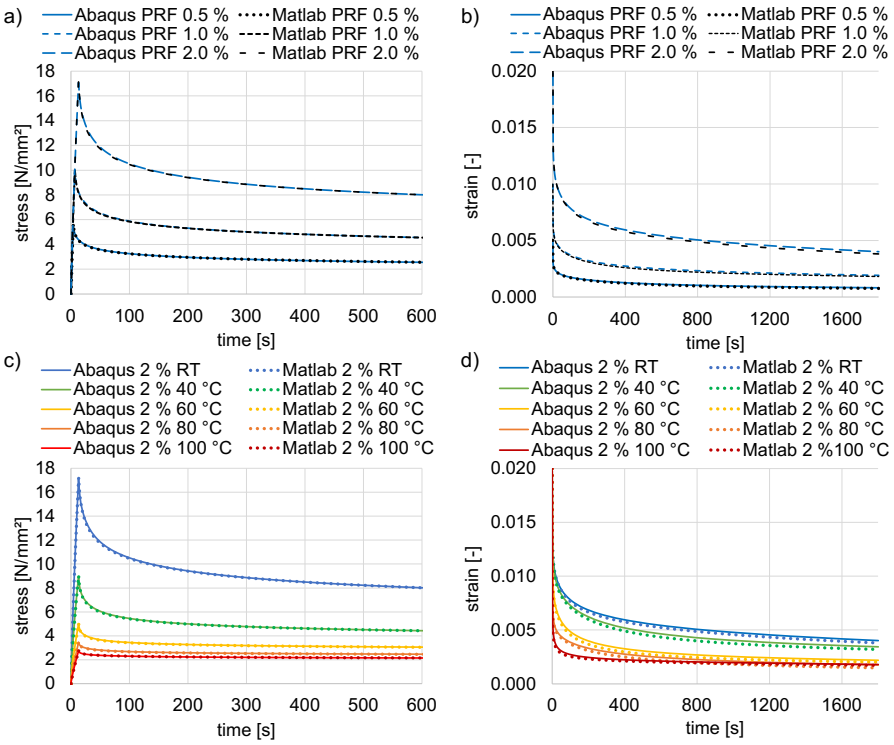

Fig. 13.10: Comparison of the results of the numerical model implemented in Matlab with an Abaqus finite element simulation at the best design point. a) Stresses of the loading phase for the three different strain levels at RT; b) Strains of the unloading phase for the three different strain levels at RT; c) Stresses of the loading phase at a strain level of 2.0 % at different temperatures; d) Strains of the unloading phase at a strain level of 2.0 % at different temperatures.

13.6 Discussion and Outlook

As shown in Table 13.3, the calibration workflow using functional relations between the parameters of the individual networks achieved the best results so far. This could be explained by the fact that a sufficient number of networks is used, whereas the amount of material parameters which need to be identified is still low. The poor results of the free calibration using only three networks (error of 20.3 %) indicate that three networks in conjunction with the Arrhenius function seem insufficient to cover the entire time and temperature range of the experiments. Increasing the amount of networks to six improves the result significantly, but the error is still twice as large as the best solution of the calibration workflow using functional relations between the parameters of the individual networks. It can be assumed that at least up to a certain point, an increasing number of networks improves the prediction accuracy of the model. However, the use of more networks is always associated with a higher amount of material parameters which need to be identified. Using a global optimization

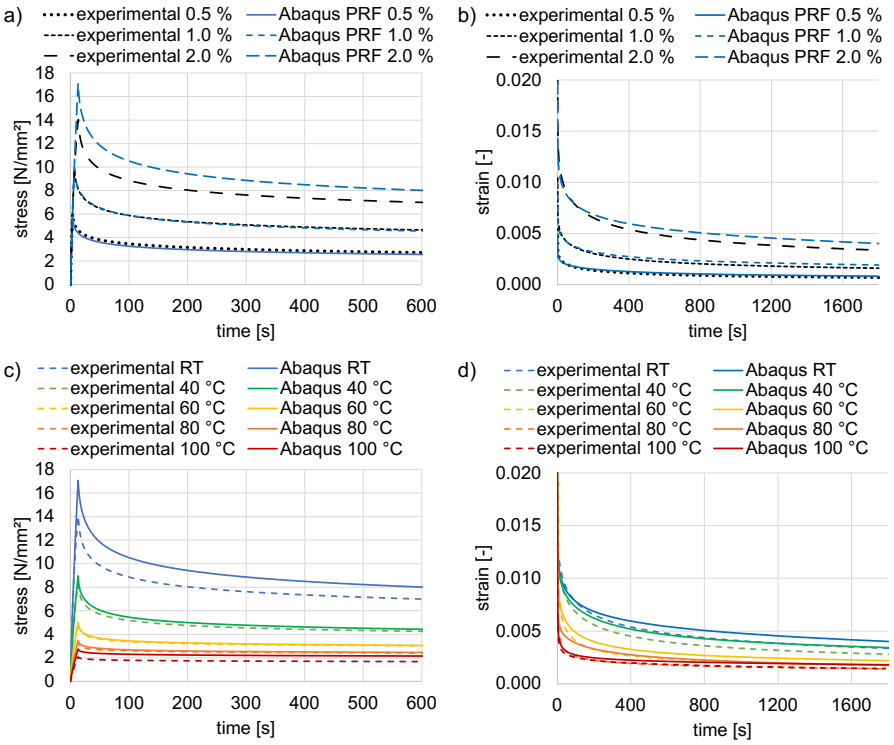

Fig. 13.11: Comparison of the Abaqus finite element simulation at the best design point with the experimental measurement data. a) Stresses of the loading phase for the three different strain levels at RT; b) Strains of the unloading phase for the three different strain levels at RT; c) Stresses of the loading phase at a strain level of 2.0 % at different temperatures; d) Strains of the unloading phase at a strain level of 2.0 % at different temperatures.

approach, the global minimum might be found with a certain probability but there is no guarantee that it is actually found by a finite number of function evaluations [27]. The fact that the use of six networks achieved a slightly better result than the use of 12 networks (Table 13.3) indicates that the number of material parameters might be too high to find a good solution using 10,000 design evaluations. In this case, a higher amount of design evaluations could be necessary. The calibration approach, which uses functional relations to describe the parameters of the networks, requires only 13 parameters regardless of the number of networks. Furthermore, a lot of parameter permutations are excluded because the parameters of the individual networks are described by continuous functions which are either increasing or decreasing. Another interesting fact is that the calibration using functional relations seems to reduce the amount of networks. In this case, the optimization was started with 19 networks but it seems that nine networks are sufficient to match the experimental data with high accuracy.

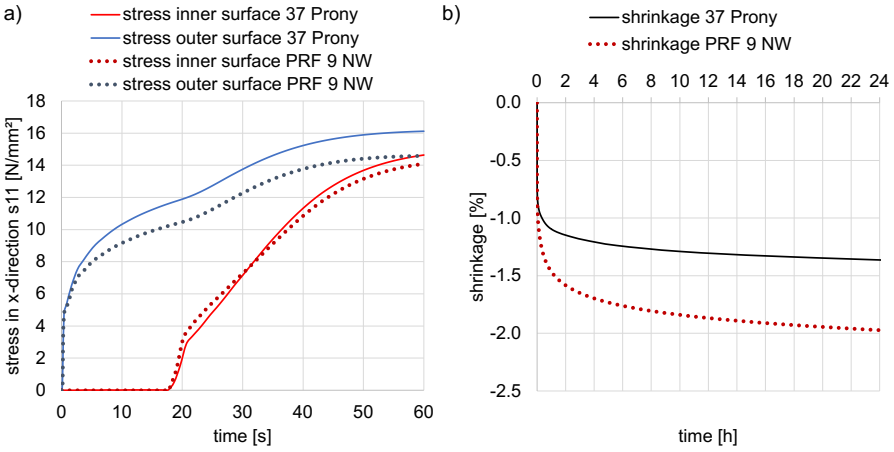

Fig. 13.12: Comparison of a one-element shrinkage analysis using a linear viscoelastic model with 37 Prony terms and the calibrated PRF model of the best design point. a) Build up of thermal stresses of the inner and outer surface during cooling under mold constraint; b) Shrinkage for a period of 24 h after demolding.

Alternatively to the use of the reduced time concept for the modeling of temperature effects, the instantaneous modulus, the stiffness ratios, and the creep model can be defined as temperature dependent by tabular values. The amount of networks necessary to cover the entire time and temperature range might be reduced in this case. However, the main advantage of the reduced time concept is that the temperature dependency is described by a continuous shift function. Thus, an extrapolation to higher temperatures seems reasonable, since the shift functions are based on experimental observations. This is essential, since experimental investigations at temperatures between 100 °C and 130 °C are difficult due to low structural stiffness at this temperature range. Nevertheless, the alternative temperature-dependent modeling using tabular values should be investigated in future work. Therefore, the use of functional relations between the parameters of the different temperature levels could also be a promising approach for a successful model calibration, especially if extrapolation to higher temperatures is necessary. In this case, the more temperature levels are tested, the better. Even if not all temperature levels are used in the model calibration, the temperature levels between the calibrated curves can be used for validation purposes. Furthermore, alternative nonlinear viscoelastic material models like the PN model provided by the PolyUMod library (PolymerFEM LLC) [20] should be investigated. One of the main disadvantages of the PRF model is that currently only isotropic thermal expansion is supported. The PN model also supports the use of constant orthotropic thermal expansion [28]. Piece-wise linear thermal expansion, which can be used to model the temperature dependency of the CTE, is currently only supported for isotropic behavior [28].

The integration of the calibrated PRF model in the shrinkage and warpage analysis leads to lower stresses during the cooling under mold constraint compared to the

linear viscoelastic model (Fig. 13.12a). This is reasonable, since the linear viscoelastic model usually overestimates the stresses at higher strain levels. Moreover, the smaller stress difference between the inner and outer surface at the time of demolding (60 s) can be explained by the fact that the inelastic strain rate increases at higher stresses, so that the relaxation will be accelerated. Nevertheless, the experimental data base which was used for the model calibration in this study is relatively small. For a successful calibration covering the entire time and temperature range of the shrinkage and warpage analysis, an extensive experimental database is needed. Additionally, the various strain levels should be investigated at all temperature levels. For a comparison of the PRF model and the linear viscoelastic model in terms of prediction accuracy, an extensive experimental database considering shrinkage and warpage is needed. The database used in [8] was limited and the part shrinkage was measured six days after demolding, so that it does not provide information about the viscoelastic retardation in the first hours after demolding. Experimental data of the dynamic shrinkage behavior of simple blow molded parts for an extensive set of process conditions, as well as experimental warpage data of complex blow molded parts could provide valuable information for the model validation.

Acknowledgements This work was funded by the German Federal Ministry of Education and Research (BMBF) within the project "Resource Optimized Forming" (ROForm) in the program FH-Kooperativ under the funding code 13FH514KX9. We would also like to thank the Graduate Institute and the TREE Institute of Hochschule Bonn-Rhein-Sieg University of Applied Sciences for supporting this work by granting a scholarship.

References

[1] Laroche D, Kabanemi KK, Pecora L, Diraddo RW (1999) Integrated numerical modeling of the blow molding process. Polymer Engineering and Science **39**(7):1223–1233

[2] Kabanemi KK, Vaillancourt H, Wang H, Salloum G (1998) Residual stresses, shrinkage, and warpage of complex injection molded products: Numerical simulation and experimental validation. Polymer Engineering and Science **38**(1):21–37

[3] Williams ML, Landel RF, Ferry JD (1955) The temperature dependence of relaxation mechanisms in amorphous polymers and other glass-forming liquids. Journal of the American Chemical Society **77**(14):3701–3707

[4] Debergue P, Massé H, Thibault F, DiRaddo R (2003) Modelling of solidification deformation in automotive formed parts. SAE Transactions **112**:359–365

[5] Benrabah Z, Debergue P, DiRaddo R (2006) Deflashing of automotive formed parts: Warpage and tolerance issues. SAE International

[6] Benrabah Z, Mir H, Zhang Y (2013) Thermo-viscoelastic model for shrinkage and warpage prediction during cooling and solidification of automotive

blow molded parts. SAE International Journal of Materials and Manufacturing **6**(2):349–364

[7] Benrabah Z, Bardetti A, Ilinca F, Ward G (2018) Numerical simulation of shrinkage and warpage deformation of an intermittent-extrusion blow molded part: validation case study. In: ANTECH 2018 Conference Proceedings, Society of Plastic Engineering. Blow Molding Division, ANTECH 2018 Conference, May 7-10, 2018, Orlando, FL, USA

[8] Michels P, Bruch O, Evers-Dietze B, Grotenburg D, Ramakers-van Dorp E, Altenbach H (2022) Shrinkage simulation of blow molded parts using viscoelastic material models. Materialwissenschaft und Werkstofftechnik **53**(4):449–466

[9] Ramakers-van Dorp E, Blume C, Haedecke T, Pata V, Reith D, Bruch O, Möginger B, Hausnerova B (2019) Process-dependent structural and deformation properties of extrusion blow molding parts. Polymer Testing **77**:105,903

[10] Grommes D, Bruch O, Geilen J (2016) Investigation of the influencing factors on the process-dependent elasticity modulus in extrusion blow molded plastic containers for material modelling in the finite element simulation. AIP Conference Proceedings **1779**(1):050,013–1–050,013–5

[11] Ramakers-van Dorp E (2019) Process-induced thermal and viscoelastic behavior of extrusion blow molded parts. PhD thesis, Tomas Bata University in Zlin, Zlin

[12] Lai J, Bakker A (1995) Analysis of the non-linear creep of high-density polyethylene. Polymer **36**(1):93–99

[13] Schapery RA (1969) On the characterization of nonlinear viscoelastic materials. Polymer Engineering and Science **9**(4):295–310

[14] Michaeli W, Brandt M, Brinkmann M, Schmachtenberg E (2006) Simulation des nicht-linear viskoelastischen Werkstoffverhaltens von Kunststoffen mit dem 3D-Deformationsmodell. Zeitschrift Kunststofftechnik **2**(5)

[15] Bergstrom JS, Bischoff JE (2010) An advanced thermomechanical constitutive model for UHMWPE. International Journal of Structural Changes in Solids – Mechanics and Applications **2**(1):31–39

[16] Lapczyk I, Hurtado JA, Govindarajan SM (2012) A parallel rheological framework for modeling elastomers and polymers. In: American Chemical Society (ed) 182nd Technical Meeting of the Rubber Division of the American Chemical Society, pp 1840–1859

[17] Hurtado J, Lapczyk I, Govindarajan S (2013) Parallel rheological framework to model non-linear viscoelasticity, permanent set and mullins effect in elastomers. In: Alonso A (ed) Constitutive Models for Rubber VIII, CRC Press, pp 95–100

[18] Dassault Systèmes (2023) SIMULIA User Assistance 2023

[19] Bergstrom J (2015) Mechanics of Solid Polymers: Theory and Computational Modeling. Elsevier, Amsterdam

[20] PolymerFEM LLC (2023) PolyUMod

[21] Gutierrez-Lemini D (2014) Engineering Viscoelasticity. Springer, New York and Heidelberg and Dordrecht and London

[22] Kipping A (2003) Thermomechanische analyse der kühlphase beim extrusionsblasformen von kunststoffen. PhD thesis, Universität Siegen, Siegen

[23] Kunststoffmaschinen VDMAFG (1979) Kenndaten für die Verarbeitung thermoplastischer Kunststoffe. Hanser, München
[24] Koppelmann J (1959) Über den dynamischen Elastizitätsmodul von Polymethacrylsäuremethylester bei sehr tiefen Frequenzen. Kolloid-Zeitschrift **164**(1):31–34
[25] Sommer W (1959) Elastisches Verhalten von Polyvinylchlorid bei statischer und dynamischer Beanspruchung. Kolloid-Zeitschrift **167**(2):97–131
[26] Kulik M (1974) Ein beitrag zur analyse des kontinuierlichen extrusionsblasformens. PhD thesis, Fak. f. Maschinenwesen, RWTH Aachen, Achen
[27] Harzheim L (2014) Strukturoptimierung: Grundlagen und Anwendungen, 2nd edn. Verlag Europa-Lehrmittel, Haan
[28] PolymerFEM LLC (2022) PolyUMod: A Library of Advanced User Materials: Version: 7.0.1